JOURNAL OF GEOPHYSICAL RESEARCH, VOL. 115, C05020, doi:10.1029/2008JC005219, 2010

Ice and ocean processes in the Bellingshausen Sea, Antarctica

Paul R. Holland,[1] Adrian Jenkins,[1] and David M. Holland[2]

Received 2 December 2008; revised 26 November 2009; accepted 4 January 2010; published 21 May 2010.

[1] In the vicinity of the Antarctic Peninsula observations show diminishing sea ice and a rapid warming of atmosphere and ocean. These changes have led to the collapse of ice shelves and retreat, acceleration, and thinning of inland ice. However, ocean observations in the center of the nearby Bellingshausen Sea are spatially and temporally coarse. In this study, ocean and sea ice models forced by atmospheric reanalyses are used to investigate this data gap by simulating processes in the Bellingshausen Sea for the years 1979–2007. The model suggests flow features in the region and predicts the basal melting of local ice shelves. Modeled ocean conditions are found to be less variable than in the nearby Amundsen Sea, which is situated closer to foci of annual and interannual atmospheric variability. Melt rates beneath George VI Ice Shelf are investigated in detail, concluding that the ice shelf may have been melting out of balance (and therefore thinning) for decades. The melt rate contains significant interannual variability that the model links to variation in sea ice conditions offshore of the southern end of the ice shelf. This stands in contrast to the Amundsen Sea, where models suggest that ice shelf melting is controlled by variable transport of Circumpolar Deep Water onto the continental shelf.

Citation: Holland, P. R., A. Jenkins, and D. M. Holland (2010), Ice and ocean processes in the Bellingshausen Sea, Antarctica, *J. Geophys. Res.*, *115*, C05020, doi:10.1029/2008JC005219.

1. Introduction

[2] Over the instrumental period the area west of the Antarctic Peninsula (Figure 1) has experienced considerable climatic changes. Data from Faraday/Vernadsky record a significant annual mean air temperature increase of 0.56°C per decade from 1951 to 2000, focused on winter with June–August temperatures rising by 1.09°C per decade [*King*, 1994; *Turner et al.*, 2005]. A smaller summer warming is implicated in the disintegration of floating ice shelves [*Vaughan and Doake*, 1996] and the acceleration and calving front retreat of nearby ice streams [*Cook et al.*, 2005; *Pritchard and Vaughan*, 2007].

[3] Bellingshausen Sea (BS) sea ice conditions, which correlate well with air temperatures on the peninsula [*King*, 1994; *Jacobs and Comiso*, 1997], have changed considerably in conjunction with this atmospheric warming. Uniquely in Antarctica, mean sea ice extent and concentration have decreased (primarily in summer) [*Stammerjohn and Smith*, 1997; *Smith and Stammerjohn*, 2001; *Liu et al.*, 2004], and the ice season duration has decreased markedly [*Parkinson*, 2002; *Stammerjohn et al.*, 2008]. The upper 100 m of the ocean has also warmed, at a rate of up to 0.5°C per decade in summer between 1955 and 1998, with the warming signal strongly surface intensified and accompanied by increasing salinity [*Meredith and King*, 2005].

[4] Several mechanisms have been suggested to explain these changes [*Vaughan et al.*, 2003]. For example, *Jacobs and Comiso* [1997] discussed the possibility that warming or increased upwelling of the Circumpolar Deep Water (CDW) present at depth in the BS could lead to a decrease in sea-ice extent and hence atmospheric warming. However, *Meredith and King* [2005] argue that the observed surface enhancement of the ocean warming signal is not explained by this process. Many authors suggest that changes in atmospheric circulation could lead to regional atmospheric warming and sea ice retreat (by mechanical drag or thermodynamic processes) [e.g., *Turner et al.*, 1997; *Marshall and King*, 1998; *Thompson and Solomon*, 2002; *Harangozo*, 2006]. However, atmospheric circulation changes explaining Antarctic Peninsula warming have not yet been detected directly. It is also possible that air-sea ice feedback has amplified these or other changes. This is supported by the winter focus of the observed warming; a midtropospheric warming similar to the summer signal is observed across Antarctica [*Turner et al.*, 2006], so a wintertime surface amplification of this signal could wholly explain the local warming.

[5] Oceanographically the BS appears similar to the Amundsen Sea (AS) further west and markedly different from other embayed shelf seas around Antarctica. The entire continental shelf is flooded by CDW (temperature ≥1.0°C, salinity 34.7) overlain by its mixtures with Winter Water (−1.5°C, 33.8–34.0) and Antarctic Surface Water (−1.8–1.0°C, 33.0–33.7) [*Talbot*, 1988; *Smith et al.*, 1999; *Jenkins and*

[1]British Antarctic Survey, Cambridge, UK.
[2]Courant Institute of Mathematical Sciences, New York University, New York, New York, USA.

0148-0227/10/2008JC005219

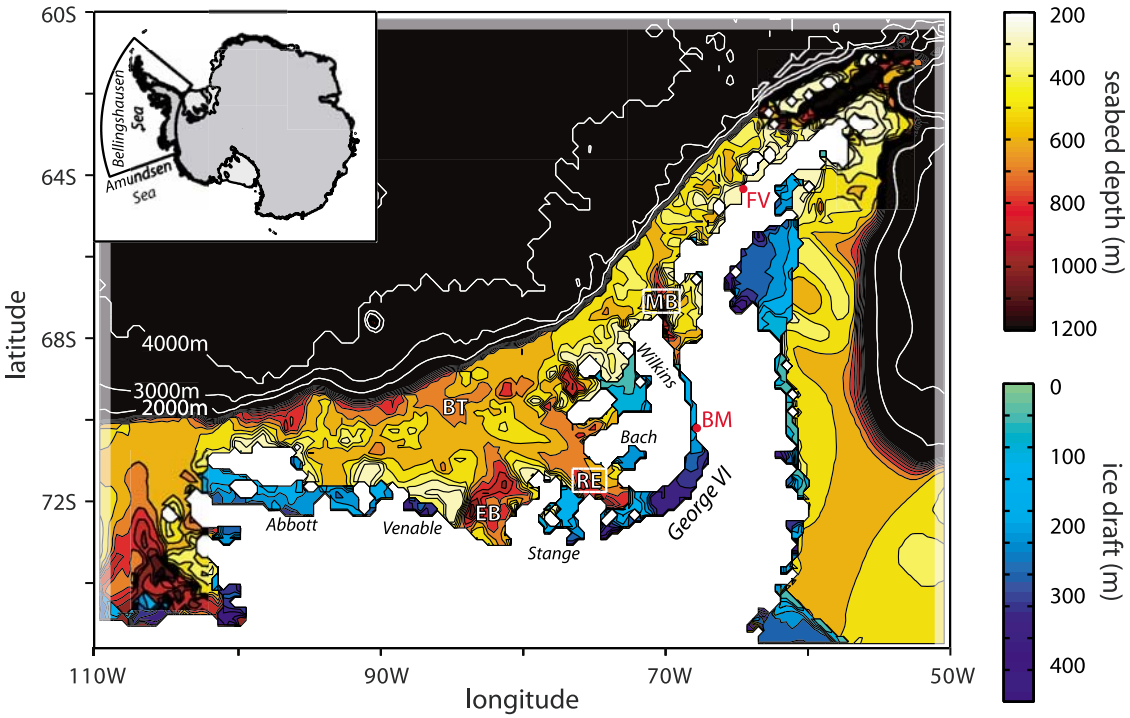

Figure 1. Model bathymetry and ice shelf thickness and location of domain (inset). Depths are contoured and colored red between 200 and 1200 m in steps of 100 m and contoured in white between 2000 and 4000 m in steps of 1000 m. Ice shelf drafts are contoured and colored blue between 0 and 450 m in steps of 50 m. Also shown are the areas over which boundary conditions are applied (faded shading around edges of domain) and model time series are calculated (white boxes). BT, Belgica Trough; EB, Eltanin Bay; RE, Ronne Entrance; MB, Marguerite Bay; FV, Faraday/Vernadsky; BM, Batterbee Mountains.

Jacobs, 2008]. The latter water masses are formed by interaction with the atmosphere, but the CDW originates in the Antarctic Circumpolar Current (ACC) offshore of the shelf break, where it is associated with a temperature maximum of 1.6–2.0°C underlain by cooler waters at a salinity maximum of 34.74. In the deep BS the temperature maximum occurs at the depth of the shelf break, so water from below often intrudes onto the shelf, giving it a discernible middepth temperature maximum [*Smith et al.*, 1999; *Klinck et al.*, 2004; *Jenkins and Jacobs*, 2008; D. R. Shoosmith, personal communication, 2008]. Intrusions of CDW onto the shelf are episodic but persistent [*Hofmann and Klinck*, 1998; *Klinck et al.*, 2004; *Moffat et al.*, 2009], can involve significant uplift of dense waters [*Klinck et al.*, 2004], and entail a ≈0.5°C cooling [*Jenkins and Jacobs*, 2008], indicating a relatively vigorous transport process.

[6] The north-eastern sector of the BS (offshore of Faraday/Vernadsky and in Marguerite Bay; see Figure 1) has been relatively well observed owing to the presence of research bases nearby [*Martinson et al.*, 2008]. The ACC flows northeast along the shelf break and CDW pulses, centered on bathymetric depressions, periodically flood onto the shelf [*Hofmann and Klinck*, 1998; *Dinniman and Klinck*, 2004; *Klinck et al.*, 2004; *Moffat et al.*, 2009; *Savidge and Amft*, 2009]. Geological evidence and near-bottom current measurements show that this flow is underlain by an opposing south-westward current tracking the continental slope [*Tucholke*, 1977; *Hillenbrand et al.*, 2008]. Thus the evidence points to vertical shear offshore of the shelf break. The circulation on shelf consists of a south-westward summertime coastal current [*Moffat et al.*, 2008] that further north may be divided into subgyres by topography [*Hofmann et al.*, 1996; *Savidge and Amft*, 2009].

[7] In contrast to this detailed picture, very little has been published on the area further west, north of Eltanin Bay and Ronne Entrance, which we hereafter refer to as the 'central BS'. *Talbot* [1988] and *Jenkins and Jacobs* [2008] report oceanographic sections from the deep ocean into Ronne Entrance, finding CDW flooding the shelf in a similar manner to further east. Seal tag observations reported by *Hofmann et al.* [2009] show that the temperature maximum is slightly cooler in the central BS than in Marguerite Bay. A variety of observations show that sea ice moves in a cyclonic fashion around this area of the shelf [*King*, 2003; *Assmann et al.*, 2005; *Heil et al.*, 2006], which suggests that the coastal current continues all the way into the AS and Ross Sea. *Orsi et al.* [1995] suggest that a current associated with the southern ACC front follows the shelf break east from 100°W, leading to the presence of core CDW offshore of the shelf break throughout the region.

[8] Many ice shelves fringe the BS (Figure 1), but the most intensively studied by far is George VI Ice Shelf (GVIIS). GVIIS occupies George VI Sound, a large rift that connects the deep continental shelf regions in Marguerite

Bay and Ronne Entrance (Figure 1). In the early 1980s the water column beneath GVIIS was sampled through rifts, revealing that CDW with temperatures of up to 1.0°C underlies the entire ice shelf [*Potter and Paren*, 1985]. At the northern end of the cavity, a CDW inflow was found to upwell and melt the ice shelf before departing in a strong surface outflow constrained to the west by Coriolis force [*Potter et al.*, 1988]. *Jenkins and Jacobs* [2008] sampled both ice fronts synoptically in 1994, finding this flow pattern at both locations and deducing a net south-to-north throughflow at the time of measurement.

[9] GVIIS basal melt rates have been determined using a variety of methods. From glaciological considerations *Bishop and Walton* [1981] determined steady state melt rates varying spatially between 1 and 8 m a^{-1}, while *Potter et al.* [1984] calculated an equilibrium rate of 2.1 m a^{-1} for the whole ice shelf. *Corr et al.* [2002] obtained a direct point measurement of 2.8 m a^{-1} total melting in December 2000 in a thick southern part of the ice shelf. *Jenkins and Jacobs* [2008] constrain the total melt rate to be between 2.3 and 4.9 m a^{-1} in March 1994, implying that on that date the ice shelf was melting above the *Potter et al.* [1984] equilibrium and losing mass. A study by L. Padman et al. (personal communication, 2009) suggests that Wilkins Ice Shelf must have melted at 1.5–2 m a^{-1} to explain their observations of ≈1 m a^{-1} thinning between 1992 and 2003. With the exception of Bach Ice Shelf, where *Woodruff and Doake* [1979] report a steady state melt rate of 0.65 m a^{-1}, we are unaware of published melt rates for other ice shelves in the area.

[10] The aim of this paper is to use a three-dimensional ocean model to extend and explain the spatially and temporally sparse observations of the BS. We suggest features of the circulation in the poorly observed central BS and nearby shelf break and examine annual and interannual variation in ocean behavior. We examine variation in the GVIIS melt rate and consider its oceanic drivers.

2. Model Description

[11] In this study atmospheric reanalysis data are used to force an isopycnic coordinate ocean model coupled to a dynamic-thermodynamic sea ice model and thermodynamically active ice shelves. The domain (Figure 1) extends from 110°W to 50°W and from 75°30′S to 60°S and all model components use an isotropic grid with a resolution of 0.4° longitude (11 km at the southern boundary, 22 km at the northern boundary). This grid is the finest that can be solved within a reasonable time; the solution is computationally intensive because a relatively large domain is required and investigating interannual variability demands a long simulation (the model generates results for the years 1979–2007 inclusive).

2.1. Ocean-Ice Shelf Model

[12] We use a version of the Miami Isopycnic Coordinate Ocean Model [*Bleck et al.*, 1992] that has been adapted for use beneath ice shelves [*Holland and Jenkins*, 2001]. The ocean is comprised of 13 isopycnic layers and a surface mixed layer that has a freely evolving density. The mixed layer handles interaction with the overlying atmosphere or ice and communicates with interior layers via an entrainment/detrainment routine. To accurately resolve the water mass structure at the continental shelf break, where rapidly varying densities overlie weakly stratified deep water [*Talbot*, 1988], the isopycnic layers are distributed evenly over a density profile comprised of two linear progressions between 1027.3 kg m^{-3} (layer 2), 1027.75 kg m^{-3} (layer 8), and 1027.875 kg m^{-3} (layer 14).

[13] Initial layer temperatures, salinities, and thicknesses are derived from the Alfred Wegener Institute (AWI) Hydrographic Atlas of the Southern Ocean [*Olbers et al.*, 1992]. On the continental shelf (defined here as all areas south of the 600 m depth contour at the continental shelf break), layer 7 is initially expanded downwards, deflating all denser layers, to ensure that subsequent shelf waters are formed by ocean processes rather than being interpolated from the atlas. The chief weakness of our modeling effort (and focus for future development) is that all model boundaries are implemented as closed nonslip walls; the impact of this should be borne in mind when considering model results. Despite this limitation a reasonable, though steady, ACC is generated offshore of the continental shelf (see section 3.3) by restoring ocean properties to the constant AWI atlas conditions over a 3 grid cell region around the western, northern, and eastern boundaries (Figure 1). Baroclinic restoring timescales vary linearly between 10 days at the outermost cells and 30 days at the innermost cells of the restoring region. No barotropic restoring is used.

[14] The bathymetric grid used in the model was formed by blending the BEDMAP bed elevation grid [*Lythe et al.*, 2001] with data compiled at the British Antarctic Survey from a variety of cruises. Ice shelf drafts are derived from the BEDMAP ice thickness. No smoothing is used on either the bedrock or ice shelf bases.

2.2. Sea-Ice Model

[15] Sea ice is modeled using version 3.14 of CICE, the Los Alamos sea ice model [*Hunke and Lipscomb*, 2006]. CICE features the elastic-viscous-plastic ice dynamics of *Hunke and Dukowicz* [1997], the energy-based ridging scheme of *Thorndike et al.* [1975], an ice strength parameterization given by *Rothrock* [1975], and horizontal advection via an incremental remapping scheme [*Lipscomb and Hunke*, 2004].

[16] The present application divides the ice into five thickness categories with lower boundaries of 0.0, 0.64, 1.39, 2.47, and 4.57 m. The energy-conserving thermodynamics model of *Bitz and Lipscomb* [1999] is used, with each thickness category using five thermodynamic layers of which the uppermost is snow. Whenever the ocean becomes supercooled, additional ice is added to the smallest size class at at rate that would quench the supercooling over a 24 hour timescale. The model starts from an ice-free state and no restoring of ice fields is applied at the edges of the domain, which are treated as nonslip solid boundaries for consistency with the ocean model.

[17] CICE contains a stability-based parameterization for the turbulent exchange of momentum and heat between atmosphere and sea ice. We replaced this with a quadratic law using a drag coefficient of 10^{-3} (a central value in the range used by other authors [*Miller et al.*, 2006]) in order to suppress spurious polynya formation, as described in the next section. Testing showed that the replacement reduced

the wind drag on the sea ice by a factor of approximately 2.5 (compared to the CICE formulation with 'standard' roughness length of 0.5 mm). Ice-water drag used a quadratic law with coefficient 6×10^{-3}.

[18] At various stages in this paper we refer to quantities derived from satellite observations of sea ice concentration. We used monthly data derived using the NASA Team algorithm [*Cavalieri et al.*, 2006] from the SMMR and SSM/I sensors over the period 1979–2007, which are henceforth referred to as 'SSMI data'. Where sea ice extent is discussed, this is the total area with ice concentration of at least 15%. See *Stammerjohn and Smith* [1996] for a full discussion of the issues involved. SSMI-derived sea ice motion vectors [*Fowler*, 2003] are also plotted for comparison with model results.

2.3. Atmospheric Forcing

[19] The model is forced with daily mean sea level pressure and 2 m air temperature from the National Centers for Environmental Prediction and National Center for Atmospheric Research (hereafter NCEP) reanalysis data [*Kalnay et al.*, 1996], interpolated to the 1 hour 'coupling' time step used to pass information between different model components. European Centre for Medium-Range Weather Forecasts reanalysis data are generally considered better in Antarctica [*Marshall*, 2003], but the NCEP reanalyses are reasonable over the satellite era [*Marshall and Harangozo*, 2000] and are the only consistent product available for the whole period of interest here. The model is run using NCEP data from 1969 onwards, but the years before 1979 are considered a spin-up period because NCEP data are significantly less reliable prior to the onset of satellite sounder data assimilation in late 1978.

[20] Sea level pressures are probably the best constrained of the reanalyses data, so these are used to calculate a geostrophic wind that is converted to a 10 m wind by applying a magnitude ratio of 0.6 and turning angle of 12° [*Thorndike and Colony*, 1982; *Timmermann et al.*, 1999]. The wind strength is ramped up over the model spin-up period to allow the deep layers on shelf to adjust from their initially deflated state. Shortwave radiation is calculated according to the formulation adopted by *Parkinson and Washington* [1979] and downwelling longwave radiation comes from the formula of *Rosati and Miyakoda* [1988]. Whenever cloud fraction is required by these formulae the climate atlas of *Oberhuber* [1988] is used. Precipitation is derived from the global climatology of *Legates and Willmott* [1990], converted to rain or snow depending upon the 2 m air temperature. Specific humidity is fixed to the saturation humidity determined by the formula of *Hunke and Holland* [2007].

[21] Early model testing revealed that the NCEP winds generated persistent wintertime polynyas in Eltanin Bay in a few specific years, leading to a prevalence of cold shelf waters in the central BS. Winter polynyas do occur in this area [*Tamura et al.*, 2008], but they are highly transient (J. C. King, personal communication, 2008) and generally do not persist for long enough to appear in the monthly SSMI data. The presence of cold waters at depth on shelf in summer directly contradicts observations, so the model polynyas are regarded as spurious. The persistent offshore winds responsible for these polynyas are questionable because the NCEP reanalysis (resolution ≈200 km) very coarsely represents the coastline and orography in the region. Excessive polynyas may partly be a feature of the sea ice model, since the lack of tensile strength in standard sea-ice rheologies makes the ice overly susceptible to shore lead polynyas [*König Beatty and Holland*, 2010]. The magnitude of the problem was exacerbated by the coarseness of sea ice grids used in early testing. We found that replacing the air-ice drag formulation as described in the previous section limited the effect of the spurious winds and reduced the formation of these polynyas to more realistic levels. This change is uncontroversial [e.g., *Miller et al.*, 2006], reduces the wind drag towards the level used in related studies [*Thoma et al.*, 2008], and produces sea-ice velocities that agree well with observations [*Heil et al.*, 2006]. We return to the topic of Eltanin Bay polynyas below.

3. Results

[22] The results of each model component are presented separately in terms of a 'snapshot' state and temporal variability. Since the observations of *Jenkins and Jacobs* [2008] were made in March 1994, this date is taken as the reference for all snapshots. The discussion proceeds down the model hierarchy from atmospheric forcing to ice shelf consequences.

3.1. Atmosphere

[23] Sea level pressures around Antarctica are dominated by the circumpolar trough, which moves south and deepens biannually in equinoctial seasons (particularly in spring) in a pattern known as the Semi-Annual Oscillation [e.g., *van Loon*, 1967]. In the South Pacific, the climatological low that is the local manifestation of this trough also undergoes a larger annual longitudinal movement between its winter location over the Ross Sea and its summer location over the BS [e.g., *Bromwich and Wang*, 2008]. Figures 2a–2d show that seasonal means of the 1979–2007 NCEP reanalysis sea level pressure used to force the model broadly bear out these patterns; the depression is centered on the BS in summer and off to the west in winter, with a deepening and southward relocation in spring. In addition, the NCEP reanalysis features a small trough centered on the BS in most seasons, most noticeably in winter.

[24] Figures 2e and 2f show climatologies of the varying air temperature and precipitation used to force the model. NCEP temperatures agree with data reported by *Vaughan and Doake* [1996] and precipitation from the data set of *Legates and Willmott* [1990] peaks on the northern peninsula in agreement with the observations and model results shown by *van Lipzig et al.* [2004]. The band of higher precipitation following the rest of the BS coastline predicted by the model of *van Lipzig et al.* [2004] is not present in our forcing, but precipitation rates over the central BS are reasonable.

3.2. Sea Ice

[25] BS sea ice varies between small areas of multiyear ice in summer to winter expanses of first year ice extending to 60°S. Figure 3 shows SSMI and model sea ice concentrations and ice motion vectors for March and September 1994,

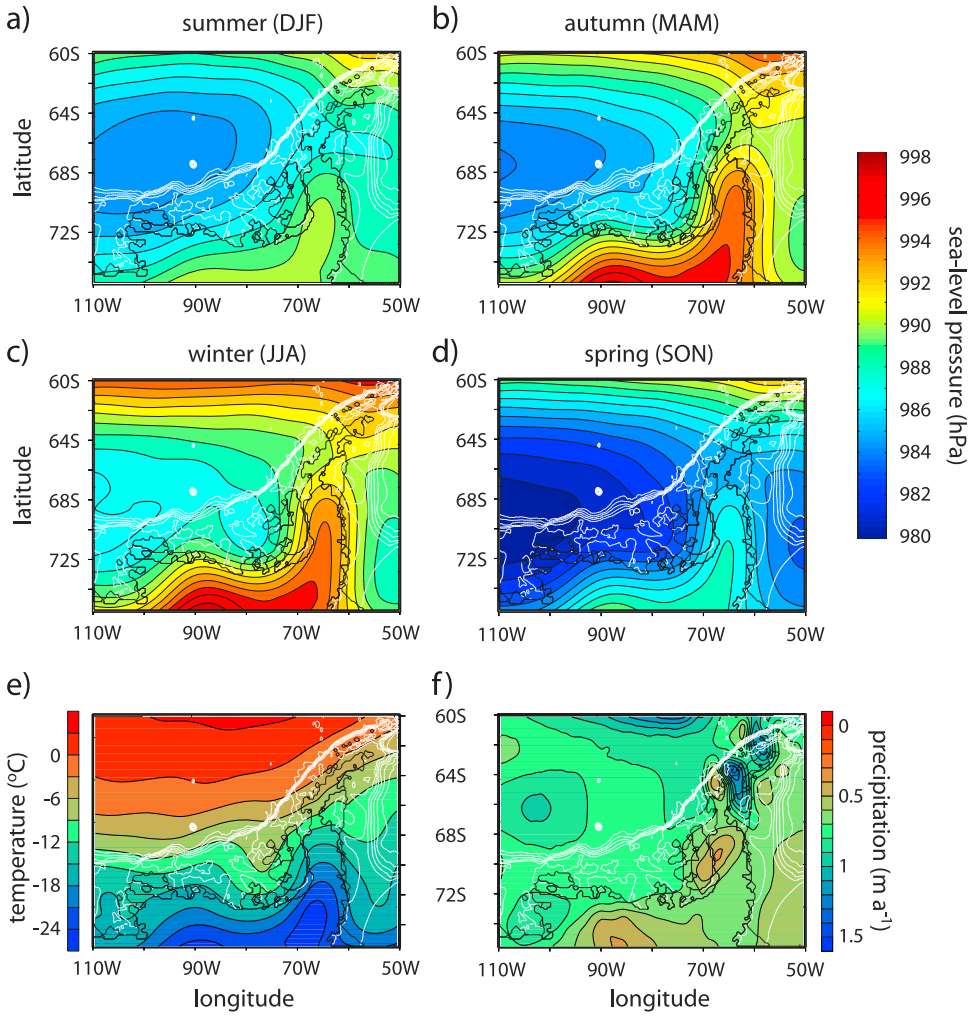

Figure 2. Atmospheric forcing averaged over the period 1979–2007. (a–d) Seasonal NCEP sea level pressure, (e) annual NCEP temperature, and (f) annual precipitation from *Legates and Willmott*'s [1990] climatology. The grounding line and ice fronts are shown in black lines, while white lines are 500 m isobaths to a depth of 3000 m.

a year of representative model skill. The agreement is generally good but with a few systematic problems.

[26] In summer, observations show that sea ice retreats to a position offshore of Abbott Ice Shelf (Figure 3), flowing westward along the coast [*King*, 2003]. The model reproduces this situation but loses its ice cover a little too rapidly, so that by March no ice remains to bound the polynyas in Ronne Entrance. Candidate explanations for this rapid retreat include excessive north-easterly winds advecting ice out of the region and overzealous melting by the atmosphere and/or ocean. There are few data against which to investigate the veracity of each mechanism, but March 2001 sea ice speeds of $\approx$30 cm s^{-1} off Venable Ice Shelf almost exactly match the buoy observations of *King* [2003]. An investigation of the full SSMI data set reveals that in spring ice generally retreats fastest in the central BS, with the southward-retreating ice edge meeting northward-growing Ronne Entrance polynyas in a band of low ice concentration. The model loses ice rapidly from a band in the correct area but does not properly reproduce the spring polynyas.

[27] The SSMI-derived ice motion vectors plotted in Figure 3 are untested in the BS and are likely to be untrustworthy in summer [*Emery et al.*, 1997]. Ice redirected northwards by our solid western boundary is melted by the atmospheric and boundary forcing (Figure 3) and very rarely enters the area of the time series discussed later. It also has little effect on ice dynamics in the center of the domain, which are basically wind driven throughout the year.

[28] The SSMI data show that in winter the central BS fills with high ice concentrations surrounded by sparser areas at the ice edge and coastline (Figure 3). As far as motion vectors can be trusted, ice drifts to the northeast, following the prevailing winds. Figure 3 shows that the model reasonably captures the overall ice extent and motion, but apparently has an excessive northward transport of ice in the central BS due to brisk south-easterly NCEP winds centered on Eltanin Bay. The persistent winter 1994 Eltanin Bay polynya is reproduced by the model (as far as it is resolved by SSMI data) despite this apparently erroneous ice motion. This polynya appears to represent a contradiction

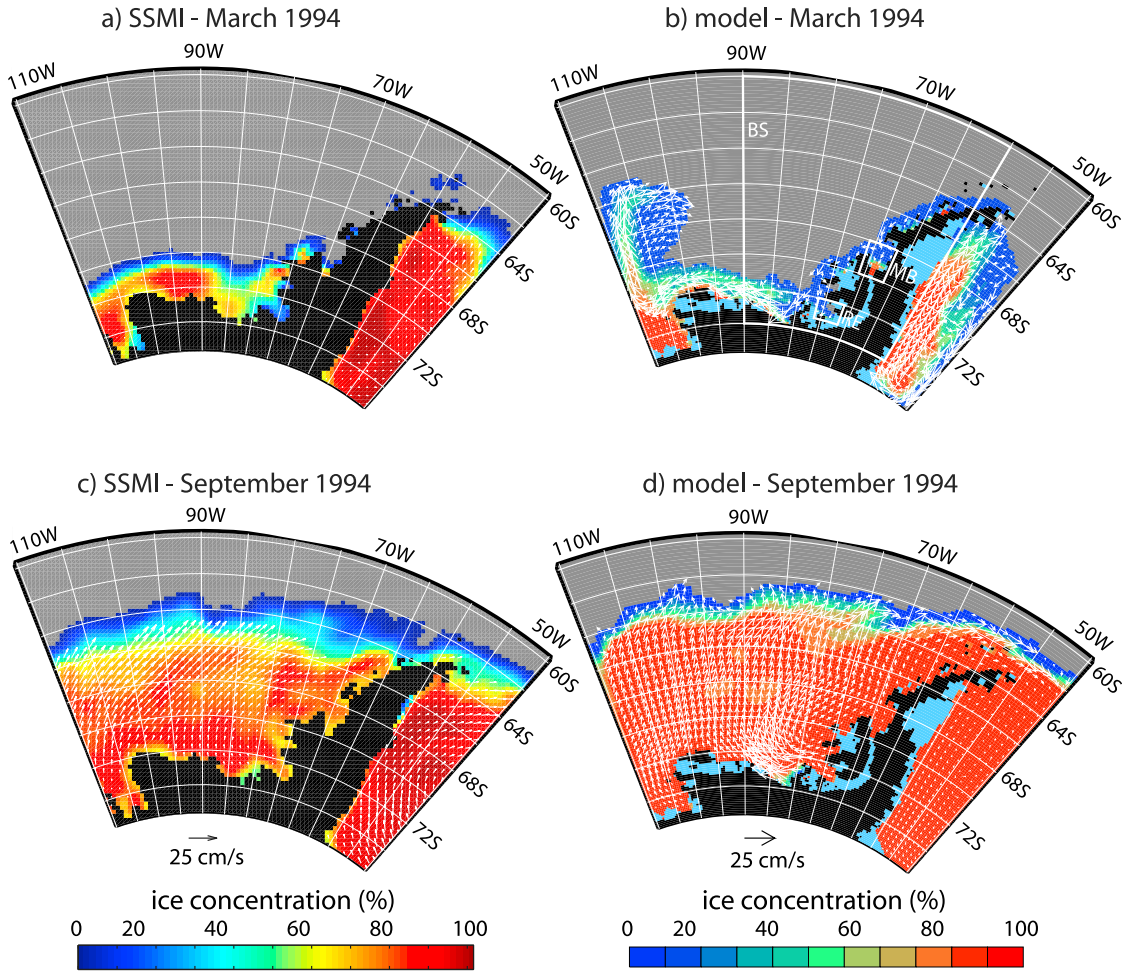

Figure 3. Comparison of (a and c) SSMI and (b and d) modeled sea ice concentrations and motion vectors for March (Figures 3a and 3b) and September (Figures 3c and 3d) 1994. Velocities are shown every second grid point in all cases. The boxes in Figure 3b show the areas over which time series of ice extent are produced in Figure 4. BS, whole Bellingshausen Sea; MB, Marguerite Bay; RE, Ronne Entrance.

between the SSMI concentration and ice motion data sets that we are unable to resolve here.

[29] Modeled ice concentrations are higher than the SSMI fields, particularly near the ice edge and coastline. The latter problem is probably due to a coarse land mask and lack of katabatics in the wind forcing. The results of *Comiso et al.* [1997] indicate that observations processed using the Bootstrap algorithm would have higher ice concentrations in the central pack, in better agreement with the model, but would retain the diffuse ice edge. Our overly sharp edge might result from excessive northward ice transport but may also be attributable to a ≈4°C cold bias in the NCEP forcing [*Bromwich and Fogt*, 2004]. (The correlation between NCEP temperatures and observations is high despite the bias (R. L. Fogt, personal communication, 2008).)

[30] Figure 4 shows a range of comparisons between SSMI and modeled ice extents designed to assess our ability to reproduce interannual sea ice variations. Inspection of the SSMI time series for the whole BS in Figure 4a shows the 1980s decline in summer sea ice extent noted by *Jacobs and Comiso* [1997] and others. It is also apparent that winter sea ice in the BS experiences significant interannual variation, expanding or contracting as the prevailing westerlies over the ice edge are moderated by meridional winds to a varying degree [*Harangozo*, 2006; *Heil et al.*, 2006]. Both the summer decline and winter variability seem to have stabilized somewhat since the mid-1990s.

[31] The model generally succeeds in reproducing interannual variability in the BS winter ice extent but never retains large areas of ice in summer (Figure 4a) in consequence of the rapid spring retreat described above. The winter maximum of the mean annual cycle is of a reasonable magnitude, though lagged behind the observations (Figure 4b). The summer minimum of the mean model cycle precedes that of the data, confirming that its underprediction arises from an excessive spring sea-ice retreat.

[32] These time series indicate that, given the quality of our forcing, the model is fairly representing large-scale sea ice processes integrated over the whole BS. Most importantly, the mean annual cycle of ice extent is reasonable and the model also captures observed interannual variations in the winter maximum (Figure 4c). It is unsurprising that ice extents are reasonable because the SST/sea ice field that forms the NCEP lower boundary condition is partly derived from SSMI data [*Kalnay et al.*, 1996]. The good correlation of winter ice extent maxima with observations gives us some

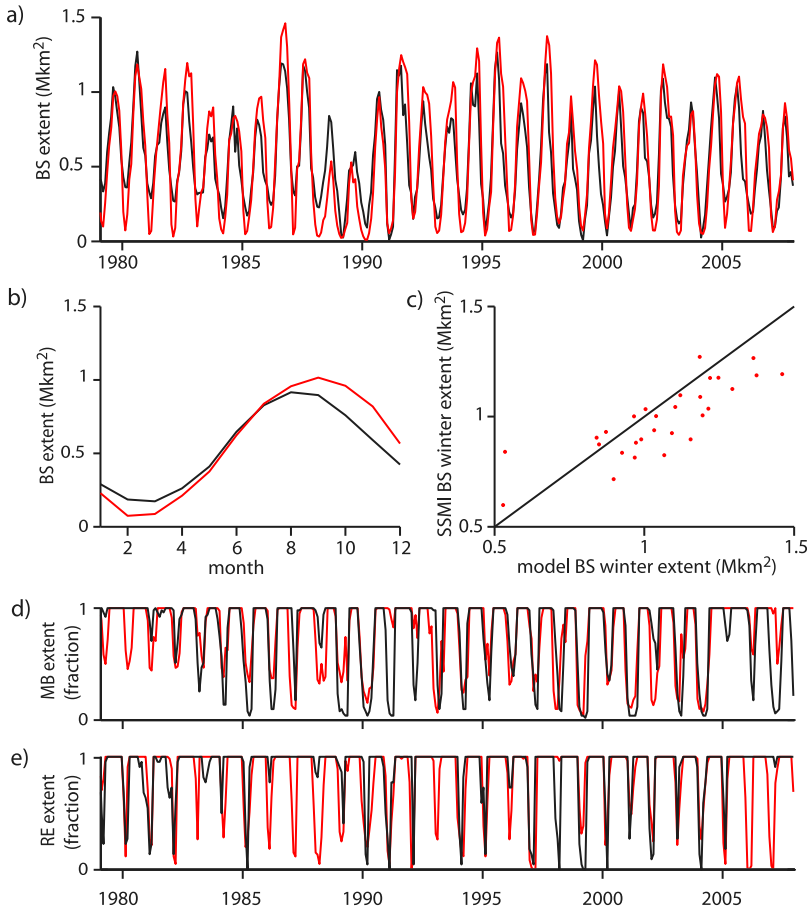

Figure 4. Comparison of temporal variation of SSMI-observed (black) and modeled (red) sea ice extent (total area with ice concentration of at least 15%) over the regions shown in Figure 3. (a) Whole BS time series of monthly ice extent, (b) 1979–2007 BS mean annual cycle, (c) observed versus modeled winter maximum BS extent (for every year each series' maximum is located independently within a 12 month window; correlation 0.82; the line represents perfect agreement), and ice extent fraction (fraction of each data set's possible ice-covered area within chosen space) in regions (d) MB and (e) RE.

confidence that interannual variations in atmospheric forcing will be transmitted to the ocean beneath, implying that we might trust interannual variability in the model ocean.

[33] Figures 4d and 4e show time series of ice extent in the bays at either end of GVIIS. These time series are expressed as fractions of possible ice-covered area because the different coastlines in the SSMI data and the model preclude a direct comparison of ice areas (this difference is negligible when the whole BS is considered). The time series show a reasonable agreement, particularly in Marguerite Bay, where the interannual variability in ice cover seems to be captured well by the model. The agreement in Ronne Entrance is less convincing, with the model predicting several retreats in years when the bay stayed ice-covered all summer. Closer investigation reveals this to be another result of the rapid central BS ice retreats described above.

3.3. Ocean

[34] Perhaps surprisingly, predicted ocean circulation patterns throughout most of the domain agree well with the available evidence despite our impermeable boundaries. A 1979–2007 average of currents at 200 m depth (Figure 5a) shows the ACC flowing eastward through the domain with a southern core that joins the shelf break (slightly too far east according to *Orsi et al.* [1995]) and follows it eastward in agreement with observation [*Dinniman and Klinck*, 2004; *Savidge and Amft*, 2009]. The model also suggests that a weak cyclonic gyre persists on the continental shelf. The deep ocean (below approximately 700 m) contains a southwestward flow that hugs contours in the continental slope (Figure 5b) in agreement with current meter observations [*Tucholke*, 1977; *Hillenbrand et al.*, 2008]. The model therefore contains vertical shear immediately offshore of the shelf break. The deep southwestward flow is probably overpredicted because our closed boundaries force a recirculation in the domain, so the layers above this are the primary focus of this study. Wherever the flow field is corrupted by closed boundaries, restoring to atlas properties ensures that no spurious water masses are formed. In particular, the recirculation on the western edge of the domain occurs over longer timescales than that of the boundary restoring, ensuring that there is no recycling of shelf water properties into the eastward-flowing ACC.

[35] Both flow patterns mentioned above persist throughout the simulation, but surface currents experience a considerable annual fluctuation due to variable wind forcing and sea

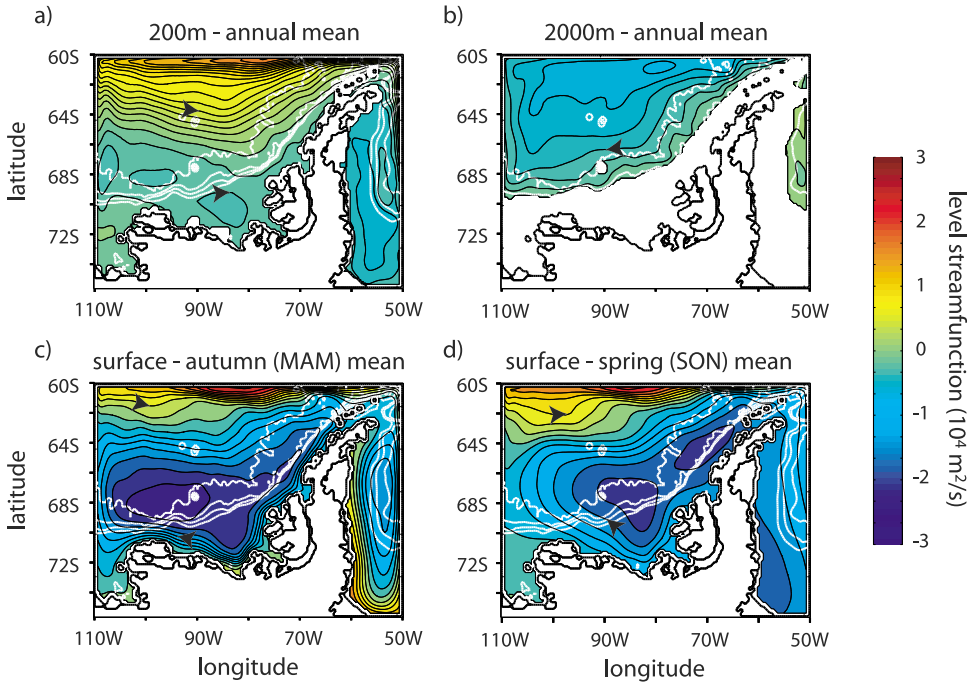

Figure 5. Contours of the two-dimensional stream function on level surfaces at various depths. (a) Long-term mean flow at 200 m, (b) long-term mean flow at 2000 m, (c) mean autumn surface flow, and (d) mean spring surface flow. The color range profiles the stream function between -3×10^4 and 3×10^4 m^2 s^{-1} with a contour spacing of 1×10^3 m^2 s^{-1} in Figures 5a and 5b and 3×10^3 m^2 s^{-1} in Figures 5c and 5d. The black lines mark the grounding line and ice fronts, and white lines are 1000 m isobaths to a depth of 4000 m. Note the effect of the closed model boundaries on ocean circulation.

ice cover. Throughout the year a strong eastward current is present north of 65°S (Figures 5c and 5d), but in autumn and summer a narrow coastal current flows south-westward along the shelf and emerges as a strong westward flow to the north of Venable and Abbott ice shelves (Figure 5c). The model thus suggests that the summertime Antarctic Peninsula Coastal Current of *Moffat et al.* [2008] extends into the central BS and increases in magnitude. The recirculation thereafter is probably a consequence of our solid western boundary; observation [*Assmann et al.*, 2005] and the atmospheric forcing (Figure 2) suggest that the coastal current should continue into the AS.

[36] *Moffat et al.* [2008] argue that the coastal current is buoyancy driven by freshwater sources. Our modeled coastal current is primarily wind driven because our precipitation climatology contains no relevant feature west of Marguerite Bay (Figure 2f) and freshwater runoff from land is neglected (though there is a minor contribution from ice shelf meltwater). Our coastal current disappears from the north-eastern BS and weakens in the central BS in winter and spring (Figure 5d) because the winds contain a smaller alongshore component in these seasons than in summer and autumn (Figure 2). The shear strength of the winter sea ice cover also increases the horizontal length over which wind stress is transmitted to the ocean, smoothing the surface flow field.

[37] Overall model results are reasonable when compared to the March 1994 observations of *Jenkins and Jacobs* [2008] (Figure 6). Salinity sections show that dense waters are bought on shelf by the model circulation, though the very densest waters with salinities greater than 34.7 are absent in the central BS because the ACC joins the shelf break a little too far east, partly bypassing Belgica Trough. In Marguerite Bay (Figure 6b) the over prevalence of dense waters and the middepth temperature maximum do not exactly match the *Jenkins and Jacobs* [2008] observations but agree with the 2001 data of *Klinck et al.* [2004], indicating that the model behavior is plausible. In both the Belgica and Marguerite sections the simulated warm surface layer is too far advanced towards the coast because of the accelerated springtime ice retreat discussed previously.

[38] In the Belgica Trough section (Figure 6a) the model does not properly raise waters from beneath the temperature maximum onto the shelf. The model also fails to represent a diapycnal mixing at the shelf break that in the observations pinches out the highest temperatures as water floods onto the shelf. Both features might in reality be related to the velocity shear at the shelf break. Water of the correct temperature gets onto the shelf but then appears to cool by ≈0.5°C relative to the observations. This cooler water is a remnant of anomalous sea ice years in the late 1980s, so we now describe the ocean's simulated interannual variability.

[39] We have shown that the model presents a reasonable ocean state and a fair expression of the surface forcing variability. Figure 7 shows that the consequent ocean variability in Ronne Entrance and Marguerite Bay, expressed as variation in isopycnic layer thicknesses, is relatively small. There are few data in Ronne Entrance with which to compare this conclusion, but several long-term monitoring projects have been carried out in and around Marguerite Bay. *Clarke*

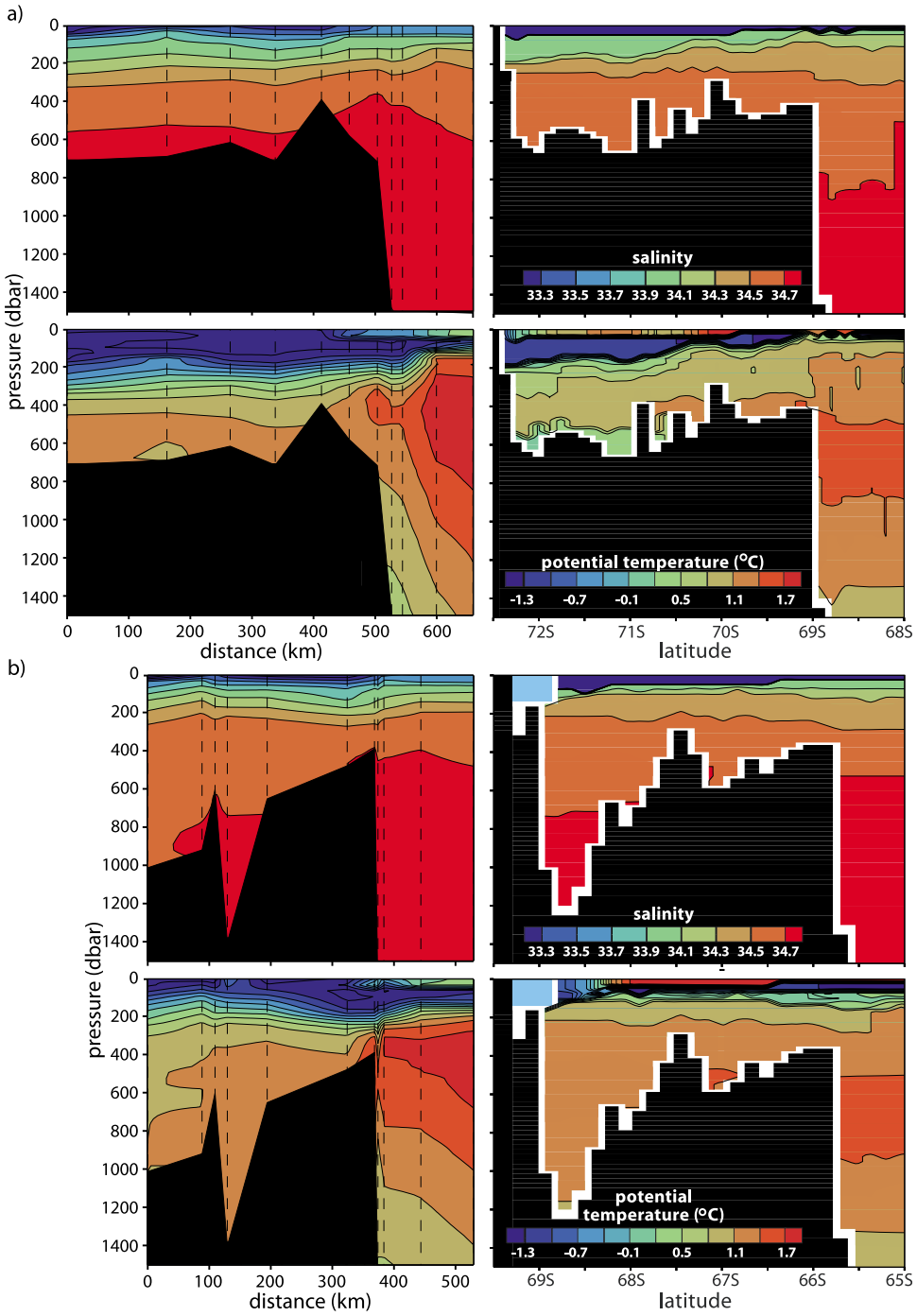

Figure 6. Comparison of (left) observed and (right) modeled salinity and temperature sections along (a) Belgica and (b) Marguerite troughs in March 1994. Note that the observations of *Jenkins and Jacobs* [2008] follow the ship track (x axis is along-track distance) while the model sections are taken along 77°30′W and 70°W (x axis is latitude).

et al. [2008] and *Klinck et al.* [2004] document significant annual variability in the upper 200 m of the water column, but *Klinck et al.* [2004] note little variation beneath this depth other than rapid periodic intrusions of CDW. *Martinson et al.* [2008] and *Clarke et al.* [2008] show that interannual variability is generally low, and basically nonexistent below 200 m. The mixed layer depths and the general lack of deep ocean variability in these studies agree with Figure 7b.

[40] Figure 7 contains considerable differences to the AS results of *Thoma et al.* [2008], despite the apparent similarity between the oceanography of that area and the BS and our use of the same ocean model, atmospheric forcing, and fixed boundary conditions. The BS results show markedly smaller mixed layer thicknesses and a reduced annual cycle in the thickness of deeper layers. There are too few data to know whether these differences are present in reality. The

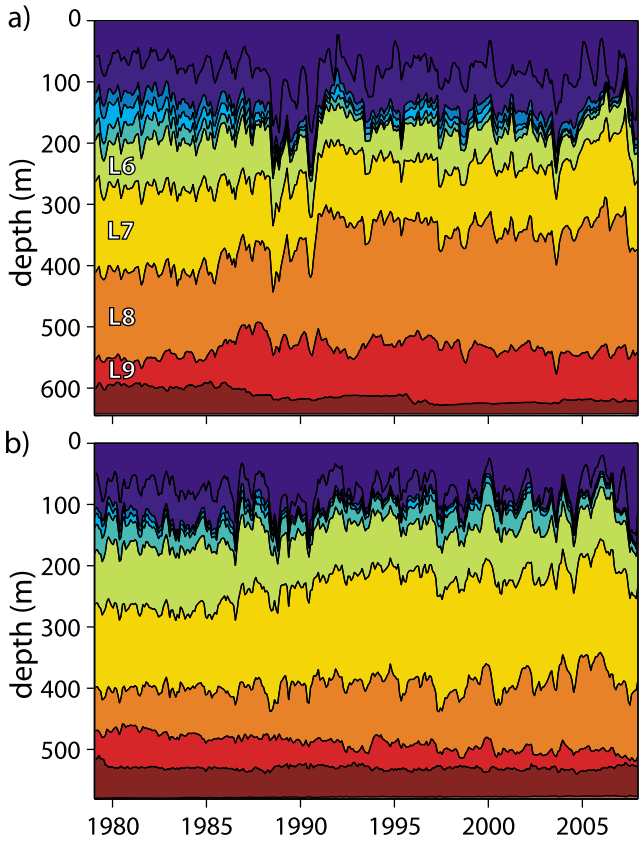

Figure 7. Time series of layer thicknesses averaged over selected areas, labeled with layer numbers. (a) Ronne Entrance (RE in Figure 1) and (b) Marguerite Bay (MB in Figure 1).

thinner mixed layers may be real but could be attributable to the improved representation of sea ice in this model; the simple ice in the *Thoma et al.* [2008] study lacks shear strength and therefore permits more polynyas and deep convection on shelf.

[41] There are good reasons to expect that the reduced annual cycle in the deep layers might be a real difference between the regions. The BS is positioned further from the center of the climatological low pressure's annual longitudinal relocation (Figure 2) so it experiences less variation in its local atmospheric forcing. The relocation causes winds over the AS shelf break to swing from easterly in summer and autumn to westerly in winter and spring. *Thoma et al.* [2008] suggest that this directly causes a springtime pulsing of CDW on shelf, with interannually-enhanced westerly flow leading to a greater CDW flux. The climatological low is always west of the BS (Figure 2), so the angle between shelf break and isobars fluctuates over a much smaller range. In consequence, less annual pulsing occurs in the on-shelf transport of CDW and the general circulation is less sensitive to interannual variations in the location of the climatological low. Variability driven by the ACC, which is precluded in both models by fixed boundary conditions, could also be important.

[42] A prominent feature of Figure 7a is the period of anomalously thick winter mixed layers in the years 1988–1991. In these years, record low sea ice extents in the BS as a whole were caused by strong winter northerlies [*Harangozo*, 2006], an effect that is exaggerated by the NCEP winds and the model (Figure 4a). During these low ice extent periods the winter ice edge lingers over the continental shelf in the central BS rather than proceeding as usual to the deep ocean, and the brine rejected by growth at the ice edge then causes anomalously deep convection on shelf (down to 400m). Ultimately this convection leads to the thickening of deep layers on shelf (Figure 7a) and the cooling noted in Figure 6a. Figure 4e shows that in these years the modeled Ronne Entrance ice extent is not anomalous, confirming that the deep mixed layers and thickened deeper layers are generated over the continental shelf rather than locally.

3.4. Ice Shelves

[43] When considering sub-ice-shelf processes we concentrate on GVIIS because the many smaller ice shelves fringing the BS are lacking in observational benchmarks and are poorly resolved by the model. *Jenkins and Jacobs* [2008] deduce that in March 1994 the circulation beneath GVIIS consisted of distinct southern and northern circulations, probably divided by a basal ridge in the ice shelf at around 70°W, superimposed upon a net northward throughflow of ≈0.22 Sv. Figure 8a shows a snapshot of the simulated mixed layer velocities from the same date, revealing that the model also features two distinct flow cells divided by the central ridge. At each end of the ice shelf, rising meltwater deflects to the left under Coriolis force. At the southern end an additional outflow occurs on the northern edge of the cavity, of which there is some evidence in the *Jenkins and Jacobs* [2008] data.

[44] Closer scrutiny of the model velocities reveals that the GVIIS cavity throughflow is incorrect, directed southward with a magnitude of 0.30 Sv. Figure 9 shows that the simulated throughflow fluctuates rapidly around a mean flow of only 0.01 Sv northward. That the flow fluctuates so widely is intriguing but impossible to assess without further data. It seems that the detail of the atmospheric forcing at either end of GVIIS determines the throughflow at a given time, so it is unsurprising that the model is unable to match observations given the coarseness of the NCEP reanalyses. It is also unsurprising that the model cannot reproduce the cavity flow when its topography is so coarsely resolved.

[45] Figure 8a also shows the pattern of melting beneath GVIIS, revealing that high melt rates are tightly focused on the deepest-drafted parts of the ice shelf near glacier inflows (Figure 1). Melt rates could be locally too high in the southern part of the ice shelf, but where the *Bishop and Walton* [1981] data exist the agreement is excellent; a local maximum melting of ≈8 m a^{-1} beneath the thick ice south of the Batterbee Mountains decreases to around 1 m a^{-1} as the ocean flows north to thinner ice. The zonal temperature section in Figure 8b shows why melting increases with ice draft; the deepest ice shelf base is bathed in warm waters that arrive at the ice shelf relatively unmodified by interaction with the atmosphere. A significant portion of the ice shelf is melted by cooler waters above these core CDW layers, which has important consequences investigated in the next section.

[46] Table 1 lists the mean and standard deviation of simulated basal melt rates for all ice shelves in the domain. These values should not be treated as reliable and are included

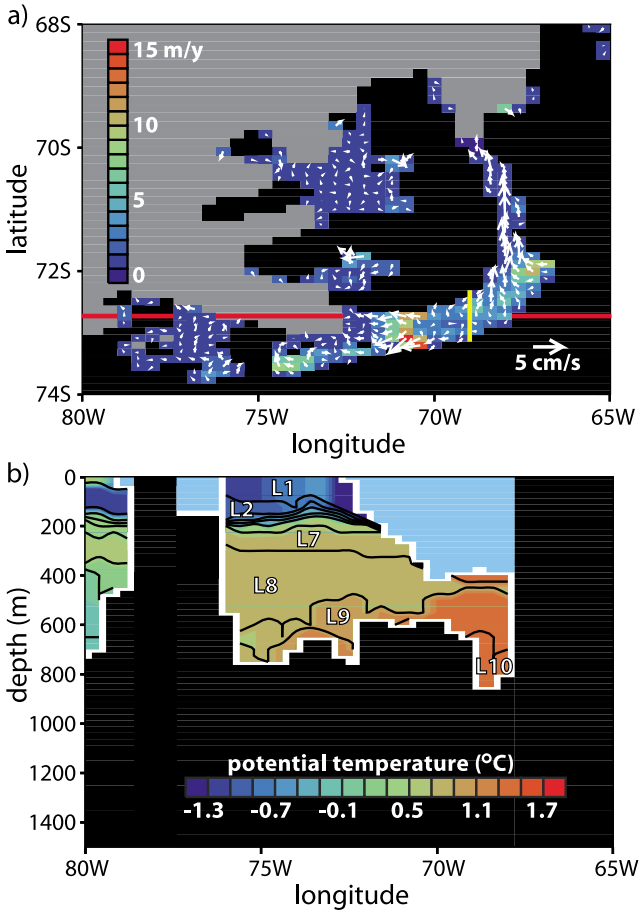

Figure 8. March 1994 conditions beneath George VI and nearby ice shelves. (a) Mixed layer velocity and basal melt rate and (b) the section along 72°45′S (the red line in Figure 8a) with potential temperatures shaded and isopycnic layers contoured. The yellow line bisects the ice shelf for Figure 11.

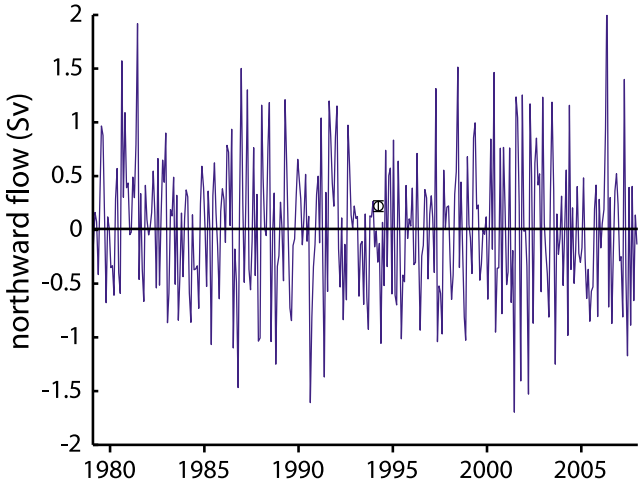

Figure 9. Time series of barotropic flow through the cavity beneath George VI Ice Shelf. Flow speeds are averaged over a longitudinal section at 71°20′S near Batterbee Mountains (see Figure 1) and converted to a volume transport using a cavity cross-sectional area of 20 km^2 estimated from the N4 traverse of *Maslanyj* [1987]. The data point is the *Jenkins and Jacobs* [2008] estimate of 0.17–0.27 Sv net flow from south to north.

partly to reveal how far grid coarseness and paucity of topographic data limits our modeling of ice shelves in this region. Some values in Table 1 are reasonable (e.g. Bach Ice Shelf, where melting exceeds the steady state 0.65 m a^{-1} of *Woodruff and Doake* [1979]) while others are less so (e.g. Wilkins Ice Shelf, where a rate of 1.5–2 m a^{-1} would be more appropriate (L. Padman, personal communication, 2009)). For the others there are no data with which to compare. It is notable that Venable Ice Shelf has a high melt rate; this and the lack of an ice shelf in Eltanin Bay are indicative that the deep water in this area is connected with the warm open ocean via Belgica Trough (Figure 1). This is a feature of great importance because satellite altimetry studies show rapid thinning of the glaciers feeding into this area [*Wingham et al.*, 2006; *Pritchard et al.*, 2009].

[47] Figure 10a shows the time series of area-averaged GVIIS melt rate throughout the simulation, which clearly falls within the range estimated by *Jenkins and Jacobs* [2008] during the period of their measurements. After 1985 the melt rate exceeds the equilibrium rate of *Potter et al.* [1984], so it could be argued that the overall results imply a thinning of GVIIS averaging 0.39 m a^{-1} from 1979–2007, or 11.21 m. The glaciological measurements used by *Potter et al.* [1984] were all taken prior to 1976, so their equilibrium rate is not strictly applicable to the predicted thinning period, but oceanographic and satellite measurements would certainly support ice shelf thinning rates of at least the magnitude shown here [*Jenkins and Jacobs*, 2008; *Pritchard et al.*, 2009; A. P. Shepherd, personal communication, 2007]. The melt rate contains significant interannual variability, including periods of several years when melting is out of balance by over 1 m a^{-1}. Factors driving variation in the melt rate are examined in the next section.

[48] Figure 10b shows that modeled net meltwater fluxes across GVIIS northern and southern ice fronts are of similar magnitude, though the southern flux increases through the simulation for reasons explained in the next section. In contrast, the 1994 data of *Jenkins and Jacobs* [2008] show that a considerably larger net meltwater flux exited the northern ice front than the southern ice front. This disagreement between model and observation is consistent with the flow discrepancy reported in Figure 9; *Jenkins and*

Table 1. Simulated Mean Melt Rates for Each Ice Shelf Fringing the Bellingshausen Sea for the Period 1979–2007[a]

Ice Shelf	Mean Melt Rate (m a^{-1})	Standard Deviation (m a^{-1})
George VI	2.49	0.67
Wilkins	0.66	0.37
Bach	1.10	0.68
Stange	0.32	0.11
Venable	3.17	1.01
Abbott	1.01	0.35

[a]Apart from George VI Ice Shelf, these values should be treated with suspicion because topographies are coarsely represented and there are few observations with which to compare results. The values illustrate that we are a considerable way from being able to reliably capture sub-ice-shelf ocean processes in this region.

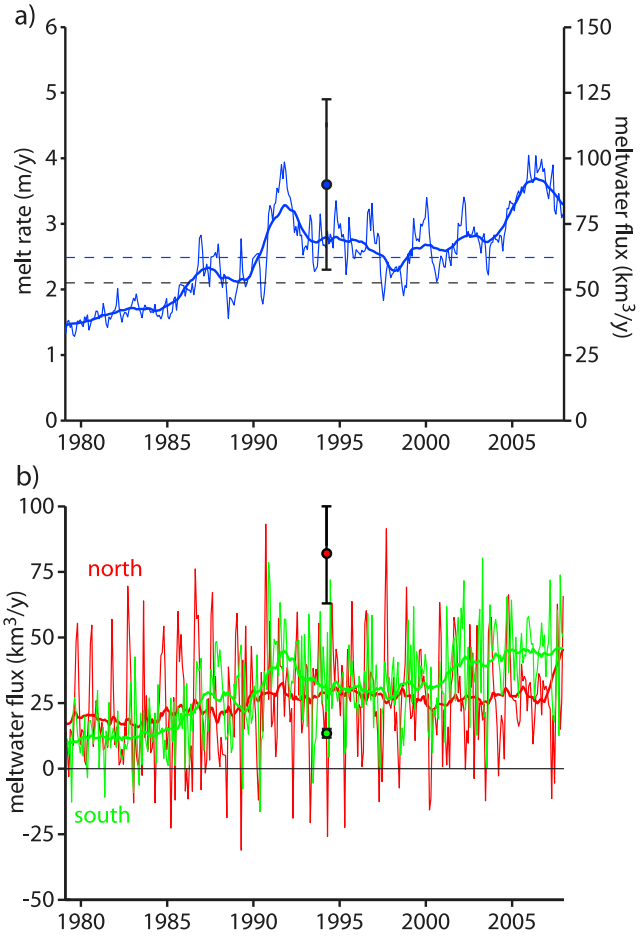

Figure 10. Time series of GVIIS melt rates and meltwater fluxes. (a) Mean basal melt rate of GVIIS. The thick line is a 2 year running mean of the same data series, and the blue dashed line is the long-term average melt rate of 2.49 m a^{-1}. The black dashed line represents the equilibrium melt rate of 2.1 m a^{-1} estimated by *Potter et al.* [1984]. The data point is the range of total melt rates consistent with the observations of *Jenkins and Jacobs* [2008]. A melt rate of 1 m a^{-1} equates to a meltwater flux of approximately 25 km^3 a^{-1} because the ice shelf area is almost exactly 25,000 km^2. (b) Net meltwater fluxes at the northern and southern ice fronts (positive oriented out of the cavity in each case). Thick lines are 2 year running means, and the data points are calculated from the observations of *Jenkins and Jacobs* [2008]. The disagreement between model and observation is caused by the lack of a net south-to-north throughflow in the model (see text).

Jacobs [2008] recorded a south-to-north throughflow that is absent in the model. *Jenkins and Jacobs* [2008] observed a large amount of meltwater entering the cavity at the southern ice front, thus decreasing its net outward flux, and if this were all carried by the throughflow it would increase the net outward meltwater flux at the northern ice front by an equal amount. Removing this contribution from both fluxes would leave them equal at approximately 45 km^3 a^{-1}. This value agrees with the results of our model, which omits the throughflow at the time in question (Figure 9). This suggests that our modeled residual melt-driven circulation is reasonable.

4. Discussion

[49] Figure 11a shows time series of melt rates averaged over the areas beneath GVIIS on either side of the 69°W meridian (as marked in Figure 8). As a result of the relative lack of variability in the deep waters in Marguerite Bay (Figure 7b), virtually all of the melting variability is driven by ocean processes at the southern end of the cavity, i.e. in the central BS. Melting in the southern sub-ice-shelf region clearly covaries with the mixed layer temperature in the same area (Figure 11b; correlation 0.91), but explaining the temperature variation is more complex. The temperatures of other layers in this region (Figure 11c) show a general rise during the early 1980s, so the mixed layer temperature (and melt rate) increases as it continually entrains those layers. The deep warming is a recovery from an event during the model spin-up, rather than purely a spin-up artifact; a similar low winter sea ice event to those of the late 1980s (see Figure 4a) occurs in 1975 and the ocean subsequently warms as cool shelf waters formed during this event are replaced by waters transported across the shelf break. The link between the cooler shelf waters in 1994 shown in Figure 6a and the late 1980s events is clearly visible in the time series of layer 7 temperature (Figure 11c). During these events cool water is injected into layer 7 over the outer shelf and then progressively advected into the areas over which Figures 6a and 11c are plotted.

[50] After 1985, fluctuations in the melt rate are caused by a different mechanism. Inspection of the layer temperatures in Figure 11c shows no trace that can explain all variations of the mixed layer temperature, such as its dip in 1989. Instead we must consider the structure of the water column offshore of the ice front, as shown in Figure 11d (a modified version of Figure 7a). Figure 11c shows that layer temperatures on shelf progressively increase with density until layers 8–10, which represent relatively unmodified CDW. Comparing the depths of layer interfaces 6/7 and 7/8 (highlighted in Figure 11d) to the mixed layer temperature (Figure 11b) an anticorrelation appears; it is clear that the mixed layer temperature (and hence the melt rate) increases whenever the deep interfaces shoal. When we also consider the maximum draft of GVIIS (Figure 11d), it becomes obvious that the melt rate peaks whenever the warm deep layers thicken to the extent that they contact the ice shelf base.

[51] This is a notable finding because the modeled variation in these layer interfaces is driven by large-scale sea ice variability in the BS rather than variations in transport at the shelf break. Water masses in layers 1–10 are advected across the shelf break, but only layers 1–8 interact with the surface via the mixed layer scheme (Figure 11c). Figure 11d shows that the intermediate water column (layers 2–8), including the layers controlling melting, fluctuates in phase with the mixed layer while the deepest layers representing unmodified CDW (9 and 10) do not. This indicates that in our model the oceanic variability affecting melting is not driven by changes in cross-shelf transport but is instead related to activity from above. Even if transport variability at the shelf

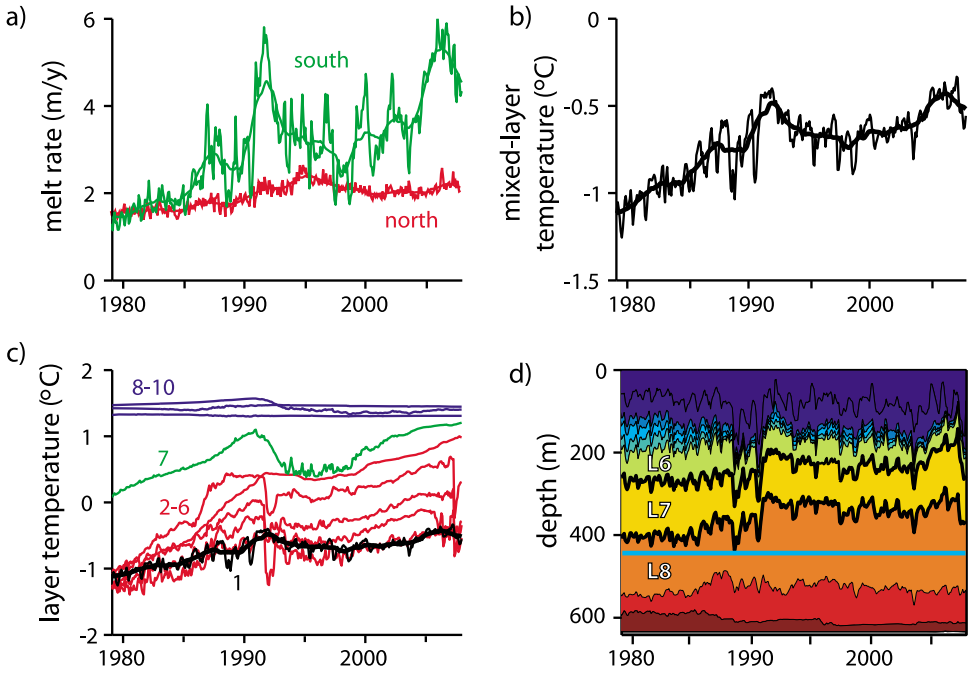

Figure 11. Time series of factors driving GVIIS basal melting. (a) Mean melt rates beneath the northern and southern parts of the ice shelf (divided by the 69°W meridian shown in Figure 8) and their 2 year running means, (b) mean mixed layer temperature in the southern region and its running mean, (c) all layer temperatures in the southern region, and (d) Ronne Entrance ocean layer structure as shown in Figure 7a (layer interfaces 6/7 and 7/8 are highlighted in bold and the horizontal line represents the maximum draft of GVIIS).

break were increased (e.g. by the addition of strong ACC variation in the boundary conditions), the intermediate layers driving melting would still be strongly impacted by on-shelf surface processes.

[52] The mixed layer thickness in Ronne Entrance features an annual cycle that is reflected in the height of the interfaces between layers 6–8 (Figure 11d). This drives an annual cycle in the mixed layer temperature under the ice shelf (Figure 11b), which translates to an annual cycle in the melt rate (Figure 11a). More importantly, Figure 11 shows considerable interannual variability adhering to the same mechanism. This is apparently driven by whole BS, rather than local, sea ice variation (compare Figure 11d with Figures 4a and 4e). As discussed in section 3.3, layers 7 and 8 are raised in the late 1980s by sea ice events that cause anomalously deep mixed layers (Figure 11d). After these events the deep mixed layer thins by detraining dense water into deep layers over the outer shelf, thickening and cooling them. This increases the melt rate overall because the thickened dense layers newly in contact with the ice base remain warmer than shallower layers despite the cooling (Figure 11c). Physically this amounts to brine rejection from sea ice growth causing open ocean convection that mixes heat upwards from the dense CDW beneath.

[53] This conclusion highlights the modeled differences between the AS and BS. Although the two regions are superficially similar, with warm CDW flooding the continental shelf, there appear to be fundamental differences in the balance of processes controlling fluctuations in the transport of CDW to ice shelf bases. Our model results suggest that variation in surface processes is more important than fluctuations in the transport of CDW onto the shelf, while the AS model application of *Thoma et al.* [2008] suggests the reverse. We also find less variability in surface processes, though this may be attributable to our use of an improved sea ice model.

[54] These conclusions are consistent with a range of differences in the external forcing of the two regions. The AS sits closer to the pole of fluctuation of the climatological atmospheric low, causing an annual pumping of warm water onto the shelf and high sensitivity to interannual variations. The BS is on the periphery of this region, implying a steadier forcing and less interannual sensitivity. In the AS the shelf break flow is uniformly westward as part of the Ross Gyre, while in the BS a westward current underlies eastward flow, producing velocity shear which may lead to increased diapycnal mixing. There are also topological differences in the ice shelves of primary interest. Simple glacier outflow ice shelves like the tongue of Pine Island Glacier have grounding lines that extend to the deepest seabed, while the drafts of 'throughflow' ice shelves like GVIIS and Wilkins only partly intrude into the water column. We have demonstrated that the latter type are physically removed from the warmest deep water masses, leading to an increased dependence of their melt rates on surface processes affecting the upper water column.

[55] There are several important caveats to the conclusions of this study. Direct comparison of our results with those of *Thoma et al.* [2008] is complicated by our usage of an improved sea ice model and slightly lower air-ice drag coefficient (10^{-3} versus 1.5×10^{-3}; air-ocean drag is 1.5×10^{-3} in both studies). Our fixed boundary conditions neglect

variability in the ACC, so important unmodeled variability could exist in the transport or properties of CDW entering the central BS; our conclusion that the BS experiences less variability than the AS refers only to local wind-driven variability in consequence. As evident from our inability to match the detail of observations at the shelf break in Figure 6, our model cannot hope to fully represent the complex processes governing on-shelf transport, which may affect our conclusions about its relative weakness. This is due to the coarse grid resolution of the model, which also limits our representation of ice shelf cavities in the region. Our annual sea-ice cycle is a little too large and the magnitude of the late 1980s events are overpredicted by the NCEP forcing, so the influence of on-shelf surface fluxes may be overestimated. However, these large events could be regarded as useful tests that impart valuable insight into the processes controlling GVIIS melt rates. Even if our representation of the processes is imperfect and the events shown here inaccurate, the general conclusion that GVIIS melt rate variation is driven from the south by sea-ice processes is logical, important, and a hypothesis to be tested by future improved models.

5. Conclusions

[56] The Antarctic Peninsula has experienced profound changes in all components of its climate, but our understanding of the nearby Bellingshausen Sea has been limited by the sparseness of observations in time and space. By applying a sea ice-ocean-ice shelf model driven by atmospheric reanalyses, we have suggested ocean processes in this area and unearthed a linkage between the oceanic melting of ice shelves and variability in the wider climate system.

[57] Modeled ocean flows corroborate and extend observations in the region, suggesting that the summer-autumn coastal current is continuous from the tip of the peninsula into the Amundsen Sea and that it might have a wind-forced component. Flow over the continental slope is north-eastward in the upper layers and south-westward beneath. Model sea ice, ocean state, and George VI Ice Shelf melt rates all agree with 'snapshot' observations taken in 1994.

[58] Good agreement between time series of simulated and observed sea ice extent implies that the atmospheric forcing contains a realistic representation of temporal variability, so we argue that we should have some confidence in the model's prediction of oceanic variability. Surface-driven annual and interannual variability in the Bellingshausen Sea is found to be considerably weaker than in the nearby Amundsen Sea. This occurs because the Bellingshausen Sea is situated at the eastern end of the climatological atmospheric low pressure that oscillates between the Ross and Amundsen seas; winds are northerly on average in all seasons. Therefore, oceanic flows are relatively persistent and insensitive to interannual fluctuations in the positioning of the climatological low.

[59] George VI Ice Shelf is the only ice shelf in the area for which there are sufficient data to calibrate the model. Our results suggest that on average it has been melting out of balance (thinning) over the simulation period. A central basal ridge divides the sub-ice-shelf circulation in two, and variations in the melt rate are found primarily to be determined by processes offshore of the southern section. The supply of heat to the ice shelf base is apparently controlled by water mass transformations effected by surface processes on the continental shelf, rather than variations in the transport of Circumpolar Deep Water from the deep ocean (although the latter are imperfectly modeled here). This is consistent with the relative steadiness of atmospheric forcing and the fact that George VI Ice Shelf intrudes less than 450 m into the water column.

[60] The observed changes in the Antarctic Peninsula climate system are a strong motivation for modeling the Bellingshausen Sea, but the reanalysis-driven models used here are unable to shed light upon mechanisms responsible for these coupled changes. Our use of solid boundaries relaxed to climatological fields means that we cannot account for the important effects of oceanic variability emanating from the Antarctic Circumpolar Current. Long simulation times and a large model domain necessitate the use of a coarse model resolution that limits our ability to model the detail of flow beneath ice shelves. Despite these important weaknesses, the study increases our understanding of the oceanography of the central Bellingshausen Sea and allows us to infer the glaciological impacts of the climatic changes that have occurred. Now that a basic oceanographic understanding of the region has been established a coupled modeling effort, using open boundary conditions and a fine model grid, is needed to fully investigate the processes responsible for climatic change in the vicinity of the Antarctic Peninsula.

[61] **Acknowledgments.** NCEP reanalysis data were provided by the NOAA/OAR/ESRL PSD, Boulder, Colorado, USA, from their web site at http://www.cdc.noaa.gov/.

References

Assmann, K., H. H. Hellmer, and S. S. Jacobs (2005), Amundsen Sea ice production and transport, *J. Geophys. Res.*, *110*, C12013, doi:10.1029/2004JC002797.

Bishop, J. F., and J. L. W. Walton (1981), Bottom melting under George VI Ice Shelf, Antarctica, *J. Glaciol.*, *27*, 429–447.

Bitz, C. M., and W. H. Lipscomb (1999), An energy-conserving thermodynamic sea ice model for climate study, *J. Geophys. Res.*, *104*, 15,669–15,677.

Bleck, R., C. Rooth, D. Hu, and L. T. Smith (1992), Salinity-driven thermocline transients in a wind- and thermohaline-forced isopycnic coordinate model of the North Atlantic, *J. Phys. Oceanogr.*, *22*, 1486–1505.

Bromwich, D. H., and R. L. Fogt (2004), Strong trends in the skill of the ERA-40 and NCEP-NCAR reanalyses in the high and midlatitudes of the Southern Hemisphere, 1958–2001, *J. Clim.*, *17*, 4603–4619.

Bromwich, D. H., and S.-H. Wang (2008), A review of the temporal and spatial variability of Arctic and Antarctic atmospheric circulation based upon ERA-40, *Dyn. Atmos. Ocean*, *44*, 213–243.

Cavalieri, D., C. Parkinson, P. Gloersen, and H. J. Zwally (2006), Sea ice concentrations from Nimbus-7 SMMR and DMSP SSM/I Passive Microwave Data, 1979–2008, http://nsidc.org/data/nsidc-0051.html, Natl. Snow and Ice Data Cent., Boulder, Colo.

Clarke, A., M. P. Meredith, M. I. Wallace, M. A. Brandon, and D. N. Thomas (2008), Seasonal and interannual variability in temperature, chlorophyll, and macronutrients in northern Marguerite Bay, Antarctica, *Deep Sea Res. Part II*, *55*, 1988–2006.

Comiso, J. C., D. J. Cavalieri, C. L. Parkinson, and P. Gloersen (1997), Passive microwave algorithms for sea ice concentration: A comparison of two techniques, *Remote Sens. Environ.*, *60*, 357–384.

Cook, A. J., A. J. Fox, D. G. Vaughan, and J. G. Ferrigno (2005), Retreating glacier fronts on the Antarctic Peninsula over the past half-century, *Science*, *308*, 541–544.

Corr, H. F. J., A. Jenkins, K. W. Nicholls, and C. S. M. Doake (2002), Precise measurement of changes in ice-shelf thickness by phase-sensitive radar to determine basal melt rates, *Geophys. Res. Lett.*, *29*(8), 1232, doi:10.1029/2001GL014618.

Dinniman, M. S., and J. M. Klinck (2004), A model study of circulation and cross-shelf exchange on the west Antarctic Peninsula continental shelf, *Deep Sea Res. Part II*, *51*, 2003–2022.

Emery, W. J., C. W. Fowler, and J. A. Maslanik (1997), Satellite-derived maps of Arctic and Antarctic sea ice motion: 1988 to 1994, *Geophys. Res. Lett.*, *24*, 897–900.

Fowler, C. (2003), Polar Pathfinder daily 25 km EASE-grid sea ice motion vectors, 1994, http://nsidc.org/data/docs/daac/nsidc0116_icemotion.gd.html, Natl. Snow and Ice Data Cent., Boulder, Colo.

Harangozo, S. A. (2006), Atmospheric circulation impacts on winter maximum sea ice extent in the west Antarctic Peninsula region (1979–2001), *Geophys. Res. Lett.*, *33*, L02502, doi:10.1029/2005GL024978.

Heil, P., C. W. Fowler, and S. E. Lake (2006), Antarctic sea-ice velocity as derived from SSM/I imagery, *Ann. Glaciol.*, *44*, 361–366.

Hillenbrand, C.-D., A. Camerlenghi, E. A. Cowan, F. J. Hernández-Molina, R. G. Lucchi, M. Rebesco, and G. Uenzelmann-Neben (2008), The present and past bottom-current flow regime around the sediment drifts on the continental rise west of the Antarctic Peninsula, *Mar. Geol.*, *255*, 55–63.

Hofmann, E. E., and J. M. Klinck (1998), Thermohaline variability of the waters overlying the west Antarctic Peninsula continental shelf, in *Ocean, Ice, and Atmosphere: Interactions at the Antarctic Continental Margin*, *Antarct. Res. Ser.*, vol. 75, edited by S. S. Jacobs and R. F. Weiss, pp. 67–81, AGU, Washington, D. C.

Hofmann, E. E., J. M. Klinck, C. M. Lascara, and D. A. Smith (1996), Water mass distribution and circulation west of the Antarctic Peninsula and including Bransfield Strait, in *Foundations for Ecological Research West of the Antarctic Peninsula*, *Antarct. Res. Ser.*, vol. 70, edited by R. M. Ross, E. E. Hofmann, and L. B. Quetin, pp. 61–80, AGU, Washington, D. C.

Hofmann, E. E., D. P. Costa, K. Daly, M. S. Dinniman, J. M. Klinck, M. Marrari, L. Padman, and A. Piñones (2009), Results from the US Southern Ocean GLOBEC synthesis studies, *GLOBEC Int. Newsl.*, *15*, 43–48.

Holland, D. M., and A. Jenkins (2001), Adaptation of an isopycnic coordinate ocean model for the study of circulation beneath ice shelves, *Mon. Weather Rev.*, *129*, 1905–1927.

Hunke, E. C., and J. K. Dukowicz (1997), An elastic-viscous-plastic model for sea ice dynamics, *J. Phys. Oceanogr.*, *27*, 1849–1867.

Hunke, E. C., and M. M. Holland (2007), Global atmospheric forcing data for Arctic ice-ocean modeling, *J. Geophys. Res.*, *112*, C04S14, doi:10.1029/2006JC003640.

Hunke, E. C., and W. H. Lipscomb (2006), *CICE: The Los Alamos Sea Ice Model Documentation and Software User's Manual*, Los Alamos Natl. Lab., Los Alamos, N. M. (Available at http://climate.lanl.gov/Models/CICE/.)

Jacobs, S. S., and J. C. Comiso (1997), Climate variability in the Amundsen and Bellingshausen seas, *J. Clim.*, *10*, 697–709.

Jenkins, A., and S. Jacobs (2008), Circulation and melting beneath George VI Ice Shelf, Antarctica, *J. Geophys. Res.*, *113*, C04013, doi:10.1029/2007JC004449.

Kalnay, E., et al. (1996), The NCEP/NCAR 40-year reanalysis project, *Bull. Am. Meteorol. Soc.*, *77*, 437–471.

King, J. C. (1994), Recent climate variability in the vicinity of the Antarctic Peninsula, *Int. J. Climatol.*, *14*, 357–369.

King, J. C. (2003), Validation of ECMWF sea level pressure analyses over the Bellingshausen Sea, Antarctica, *Weather Forecasting*, *18*, 536–540.

Klinck, J. M., E. E. Hofmann, R. C. Beardsley, B. Salihoglu, and S. Howard (2004), Water-mass properties and circulation on the west Antarctic Peninsula continental shelf in austral fall and winter 2001, *Deep Sea Res. Part II*, *51*, 1925–1946.

König Beatty, C., and D. M. Holland (2010), Modeling landfast sea ice by adding tensile strength, *J. Phys. Oceanogr.*, *40*, 185–198, doi:10.1175/2009JPO4105.1.

Legates, D. R., and C. J. Willmott (1990), Mean seasonal and spatial variability in gauge-corrected global precipitation, *Int. J. Climatol.*, *10*, 111–127.

Lipscomb, W. H., and E. C. Hunke (2004), Modeling sea ice transport using incremental remapping, *Mon. Weather Rev.*, *132*, 1341–1354.

Liu, J., J. A. Curry, and D. G. Martinson (2004), Interpretation of recent Antarctic sea ice variability, *Geophys. Res. Lett.*, *31*, L02205, doi:10.1029/2003GL018732.

Lythe, M. B., et al. (2001), BEDMAP: A new ice thickness and subglacial topographic model of Antarctica, *J. Geophys. Res.*, *106*, 11,335–11,351.

Marshall, G. J. (2003), Trends in the Southern Annular Mode from observations and reanalyses, *J. Clim.*, *16*, 4134–4143.

Marshall, G. J., and S. H. Harangozo (2000), An appraisal of NCEP/NCAR reanalyses MSLP data viability for climate studies in the South Pacific, *Geophys. Res. Lett.*, *27*, 3057–3060.

Marshall, G. J., and J. C. King (1998), Southern Hemisphere circulation anomalies associated with extreme Antarctic Peninsula winter temperatures, *Geophys. Res. Lett.*, *25*, 2437–2440.

Martinson, D. G., S. E. Stammerjohn, R. A. Ianuzzi, R. C. Smith, and M. Vernet (2008), Western Antarctic Peninsula physical oceanography and spatio-temporal variability, *Deep Sea Res. Part II*, *55*, 1964–1987, doi:10.1016/j.dsr2.2008.04.038.

Maslanyj, M. P. (1987), Seismic bedrock depth measurements and the origin of George VI Sound, Antarctic Peninsula, *Br. Antarct. Surv. Bull.*, *75*, 51–65.

Meredith, M. P., and J. C. King (2005), Rapid climate change in the ocean west of the Antarctic Peninsula during the second half of the 20th century, *Geophys. Res. Lett.*, *32*, L19604, doi:10.1029/2005GL024042.

Miller, P. A., S. W. Laxon, D. L. Feltham, and D. J. Cresswell (2006), Optimization of a sea ice model using basinwide observations of Arctic sea ice thickness, extent, and velocity, *J. Clim.*, *19*, 1089–1108.

Moffat, C., R. C. Beardsley, B. Owens, and N. van Lipzig (2008), A first description of the Antarctic Peninsula Coastal Current, *Deep Sea Res. Part II*, *55*, 277–293.

Moffat, C., B. Owens, and R. C. Beardsley (2009), On the characteristics of Circumpolar Deep Water intrusions to the west Antarctic Peninsula continental shelf, *J. Geophys. Res.*, *114*, C05017, doi:10.1029/2008JC004955.

Oberhuber, J. M. (1988), An atlas based on COADS data set, *Tech. Rep. 15*, Max-Planck-Inst. für Meteorol., Hamburg, Germany. (Available at http://gcmd.nasa.gov/records/GCMD_MPI_FLUX.html.)

Olbers, D., V. Gouretski, G. Seiss, and J. Schröter (1992), Hydrographic Atlas of the Southern Ocean, http://gcmd.nasa.gov/records/GCMD_AWI-SODB.html, Alfred Wegener Inst., Bremerhaven, Germany.

Orsi, A. H., T. Whitworth, and W. D. Nowlin (1995), On the meridional extent and fronts of the Antarctic Circumpolar Current, *Deep Sea Res. Part I*, *42*, 641–673.

Parkinson, C. L. (2002), Trends in the length of the Southern Ocean sea-ice season, 1979–99, *Ann. Glaciol.*, *34*, 435–440.

Parkinson, C. L., and W. M. Washington (1979), A large-scale numerical model of sea ice, *J. Geophys. Res.*, *84*, 311–336.

Potter, J. R., and J. G. Paren (1985), Interaction between ice shelf and ocean in George VI Sound, Antarctica, in *Oceanology of the Antarctic Continental Shelf*, *Antarct. Res. Ser.*, vol. 43, edited by S. S. Jacobs, pp. 35–58, AGU, Washington, D. C.

Potter, J. R., J. G. Paren, and J. Loynes (1984), Glaciological and oceanographic calculations of the mass balance and oxygen isotope ratio of a melting ice shelf, *J. Glaciol.*, *30*, 161–170.

Potter, J. R., M. H. Talbot, and J. G. Paren (1988), Oceanic regimes at the ice fronts of George VI Sound, Antarctic Peninsula, *Cont. Shelf Res.*, *8*, 347–362.

Pritchard, H. D., and D. G. Vaughan (2007), Widespread acceleration of tidewater glaciers on the Antarctic Peninsula, *J. Geophys. Res.*, *112*, F03S29, doi:10.1029/2006JF000597.

Pritchard, H. D., R. J. Arthern, D. G. Vaughan, and L. A. Edwards (2009), Extensive dynamic thinning on the margins of the Greenland and Antarctic ice sheets, *Nature*, *461*, 971–975, doi:10.1038/nature08471.

Rosati, A., and K. Miyakoda (1988), A general ocean circulation model for upper ocean simulation, *J. Phys. Oceanogr.*, *18*, 1601–1626.

Rothrock, D. A. (1975), The energetics of the plastic deformation of pack ice by ridging, *J. Geophys. Res.*, *80*, 4514–4519.

Savidge, D. K., and J. A. Amft (2009), Circulation on the west Antarctic Peninsula derived from 6 years of shipboard ADCP transects, *Deep Sea Res. Part I*, *56*, 1633–1655, doi:10.1016/j.dsr.2009.05.011.

Smith, D. A., E. E. Hofmann, J. M. Klinck, and C. M. Lascara (1999), Hydrography and circulation of the west Antarctic Peninsula continental shelf, *Deep Sea Res. Part I*, *46*, 925–949.

Smith, R. C., and S. E. Stammerjohn (2001), Variations of surface air temperature and sea-ice extent in the western Antarctic Peninsula region, *Ann. Glaciol.*, *33*, 493–500.

Stammerjohn, S. E., and R. C. Smith (1996), Spatial and temporal variability of western Antarctic Peninsula sea ice coverage, in *Foundations for Ecological Research West of the Antarctic Peninsula*, *Antarct. Res. Ser.*, vol. 70, edited by R. M. Ross, E. E. Hofmann, and L. B. Quetin, pp. 81–104, AGU, Washington, D. C.

Stammerjohn, S. E., and R. C. Smith (1997), Opposing Southern Ocean climate patterns as revealed by trends in regional sea ice coverage, *Clim. Change*, *37*, 617–639.

Stammerjohn, S. E., D. G. Martinson, R. C. Smith, X. Yuan, and D. Rind (2008), Trends in Antarctic annual sea ice retreat and advance and their relation to El Ni no–Southern Oscillation and Southern Annular Mode variability, *J. Geophys. Res.*, *113*, C03S90, doi:10.1029/2007JC004269.

Talbot, M. H. (1988), Oceanic environment of George VI Ice Shelf, Antarctic Peninsula, *Ann. Glaciol.*, *11*, 161–164.

Tamura, T., K. I. Ohshima, and S. Nihashi (2008), Mapping of sea ice production for Antarctic coastal polynyas, *Geophys. Res. Lett.*, *35*, L07606, doi:10.1029/2007GL032903.

Thoma, M., A. Jenkins, D. Holland, and S. Jacobs (2008), Modelling Circumpolar Deep Water intrusions on the Amundsen Sea continental shelf, Antarctica, *Geophys. Res. Lett.*, *35*, L18602, doi:10.1029/2008GL034939.

Thompson, D. W. J., and S. Solomon (2002), Interpretation of recent Southern Hemisphere climate change, *Science*, *296*, 895–899.

Thorndike, A. S., and R. Colony (1982), Sea ice motion in response to geostrophic winds, *J. Geophys. Res.*, *87*, 5845–5852.

Thorndike, A. S., D. A. Rothrock, G. A. Maykut, and R. Colony (1975), The thickness distribution of sea ice, *J. Geophys. Res.*, *80*, 4501–4513.

Timmermann, R., P. Lemke, and C. Kottmeier (1999), Formation and maintenance of a polynya in the Weddell Sea, *J. Phys. Oceanogr.*, *29*, 1251–1264.

Tucholke, B. E. (1977), Sedimentation processes and acoustic stratigraphy in the Bellingshausen basin, *Mar. Geol.*, *25*, 209–230.

Turner, J., S. R. Colwell, and S. Harangozo (1997), Variability of precipitation over the coastal western Antarctic Peninsula from synoptic observations, *J. Geophys. Res.*, *102*, 13,999–14,007.

Turner, J., S. R. Colwell, G. J. Marshall, T. A. Lachlan-Cope, A. M. Carleton, P. D. Jones, V. Lagun, P. A. Reid, and S. Iagovkina (2005), Antarctic climate change during the last 50 years, *Int. J. Climatol.*, *25*, 279–294.

Turner, J., T. A. Lachlan-Cope, S. Colwell, G. J. Marshall, and W. M. Connolley (2006), Significant warming of the Antarctic winter troposphere, *Science*, *311*, 1914–1917.

van Lipzig, N. P. M., J. C. King, T. A. Lachlan-Cope, and M. R. van den Broeke (2004), Precipitation, sublimation, and snow drift in the Antarctic Peninsula region from a regional atmospheric model, *J. Geophys. Res.*, *109*, D24106, doi:10.1029/2004JD004701.

van Loon, H. (1967), The half-yearly oscillations in middle and high southern latitudes and the coreless winter, *J. Atmos. Sci.*, *24*, 472–486.

Vaughan, D. G., and C. S. M. Doake (1996), Recent atmospheric warming and retreat of ice shelves on the Antarctic Peninsula, *Nature*, *379*, 328–331.

Vaughan, D. G., G. J. Marshall, W. M. Connolley, C. Parkinson, R. Mulvaney, D. A. Hodgson, J. C. King, C. J. Pudsey, and J. Turner (2003), Recent rapid regional climate warming on the Antarctic Peninsula, *Clim. Change*, *60*, 243–274.

Wingham, D. J., A. Shepherd, A. Muir, and G. J. Marshall (2006), Mass balance of the Antarctic Ice Sheet, *Philos. Trans. R. Soc. London Ser. A*, *364*, 1627–1635, doi:10.1098/rsta.2006.1792.

Woodruff, A. H. W., and C. S. M. Doake (1979), Depolarization of radio waves can distinguish between floating and grounded ice sheets, *J. Glaciol.*, *23*, 223–232.

D. M. Holland, Courant Institute of Mathematical Sciences, New York University, Mail Code 0711, 251 Mercer St., New York, NY 10012-1185, USA. (holland@cims.nyu.edu)

P. R. Holland and A. Jenkins, British Antarctic Survey, High Cross, Madingley Road, Cambridge CB3 0ET, UK. (p.holland@bas.ac.uk; ajen@bas.ac.uk)